Numerical Investigation of Propeller-Wing Interaction Noise with Scattering and Shielding

Maks J. Groom* and Beckett Y. Zhou†
Daniel Guggenheim School of Aerospace Engineering, Georgia Institute of Technology
Montgomery Knight Building, 270 Ferst Dr, Atlanta, GA 30332

Leonard V. Lopes‡
Aeroacoustics Branch, NASA Langley Research Center, Hampton, Virginia 23681

Aerodynamic and acoustic interactions in installed propeller configurations can have significant effects on overall noise levels. In this paper, we present a mid-fidelity approach that combines a panel-vortex particle method for aerodynamic prediction with a novel time domain boundary element method (TDBEM) for acoustic prediction to efficiently resolve installation effects on tonal noise. The approach is applied to a propeller-wing configuration originally presented and tested by Zawodny et al. (2021) [1]. Aerodynamic and acoustic predictions are compared against experimental data to assess the proposed approach, as well as to investigate the interactional mechanisms responsible for the far-field noise. The results show strong potential to capture interaction noise, although some discrepancies remain for aspects of the unsteady aerodynamic and acoustic predictions at certain wing placements. Breakdowns of acoustic contributions in the installed propeller configurations reveal significant effects from propeller potential interaction, wake impingement, and scattering mechanisms. The near-field spatial scaling of the propeller acoustic field with the propeller diameter is observed to have a strong impact on the scattering effect from the wing, leading to a significant scattered contribution even though the far-field acoustic wavelength is much larger than the wing chord.

I. Introduction

Recent interest in propeller-driven electric vertical takeoff and landing (eVTOL) concepts has highlighted the importance of aerodynamically generated noise as a significant design consideration for many aircraft. Particularly in urban settings, reducing noise levels is a priority for mitigating adverse health and environmental impacts and improving public acceptability [2]. It is therefore increasingly important to develop computationally efficient numerical capabilities to model noise sources as early as possible in the design process.

Compared to isolated propellers and rotors, installed propeller configurations introduce additional interactional noise sources. Installation effects include aerodynamic interactions that create noise sources due to wake impingement and potential interactions, as well as acoustic installations that affect propagation, namely scattering and shielding by vehicle surfaces. A characterization of the combined effects of all interaction phenomena is necessary to inform design choices, and there is a need for computationally efficient noise prediction tools that can assess contributions from both aerodynamic and acoustic interactions for complete installed propeller configurations.

To resolve interactional noise sources, coupled CFD-CAA methods are typically applied to solve for the near-field flow and propagate acoustic pressure signals from the near-field sources to the far field. Most work on installed propeller configurations has focused on the use of high-fidelity CFD techniques, including large eddy simulation (LES) methods [3], unsteady Reynolds-averaged Navier Stokes (URANS) methods [1], and hybrid RANS/LES methods such as detached eddy simulation [4, 5]. While these methods demonstrate good accuracy, they remain prohibitive for early design stages and multi-query tasks such as design optimization. Mid-fidelity simulation techniques based on inviscid panel methods coupled to vortex particle method (VPM) wake models provide a computationally efficient alternative capable of resolving key unsteady flow features. These methods are particularly suited to efficient modeling of unsteady wake interactions because they represent compact vortical structures without dissipation artifacts and do not require a volume mesh. Panel-VPM solvers have previously been applied to prediction of isolated and installed propeller

*Graduate Student, AIAA Student Member; mgroom@gatech.edu
†Assistant Professor, AIAA Senior Member; beckett.zhou@gatech.edu
‡Senior Research Engineer, AIAA Member; leonard.v.lopes@nasa.gov.

tonal noise [6–9] coupled with boundary integral formulations of the Ffowcs Williams-Hawkings (FWH) aeroacoustic analogy [10].

Despite encouraging results for capturing interactional noise sources through CFD-aeroacoustic analogy methods in general and panel-VPM with FWH in particular, scattering and shielding effects are typically neglected by widely-used aeroacoustic analogy approaches [11]. In some cases, scattering and shielding can be captured directly if high-fidelity compressible computational fluid dynamics (CFD) simulations are used to obtain an acoustically resolved field, and all noise sources are subsequently included in the integration [12]. However, resolution of acoustic propagation within compressible CFD simulations is severely limited by numerical dissipation artifacts, contamination, and computational constraints [13]. Additionally, many CFD methods that are applied to propeller noise prediction are inherently unable to resolve acoustic propagation directly, including incompressible CFD [14], URANS, and mid-fidelity panel-VPM approaches. As a result, scattering and shielding effects frequently require a separate computation. A recent review of urban air mobility (UAM) noise research by Rizzi et al. [2] highlighted the need for robust, integrated scattering approaches to address a gap in current noise prediction methodologies.

There are several approaches for including scattering and shielding effects in acoustic propagation, all with strengths for different applications. Grid-based methods, which solve propagation equations such as the acoustic perturbation equations (APE) [15], offer the greatest accuracy and flexibility for boundary conditions, background flows, and acoustic source representations. However, they require a volume grid over the entire domain, which is computationally prohibitive for an early design and optimization tool. Geometrical acoustics (GA) methods [16] approximate acoustic waves as particles that propagate along rays, with models for diffraction along smooth surfaces and at sharp edges. This approximation is formally valid in the high frequency limit and applies to propagation from frame-fixed sources. Frequency domain boundary element methods [17] solve the Helmholtz equation at a single harmonic frequency for a frame-fixed source distribution. These methods are accurate at all frequencies; however, the computational complexity increases rapidly, limiting attainable frequencies, and broadband sources require separate computations at each frequency of interest. Time domain boundary element methods [18, 19] (TDBEM) solve the acoustic wave equation, allowing efficient simulation of transient sources, including arbitrarily moving or rotating source distributions. While implementation of TDBEMs is difficult due to the 3+1 dimensional spacetime setting, they include all frequencies in a signal together in a single computation. Equivalent source methods (ESM) are similar to BEMs, with both frequency domain [20] and time domain [21] formulations, and many of the same strengths and limitations. In contrast to BEMs that solve for layer potentials distributed on the scattering surface, ESMs represent the scattered field using equivalent sources located inside a scattering body. This simplifies the numerical implementation at the cost of degraded performance for thin bodies and near edges, additional free parameters (including source positions) that must be tuned to different geometries, and reliance on ad hoc stabilization methods [22].

Scattering of installed propeller noise, especially at early design stages, has some specific constraints compared to other types of noise sources. In particular, propellers are rotating, broadband noise sources, with significant low frequency content. For configurations with wings as a significant scattering surface, it is important to accurately model thin surfaces with sharp trailing edges. Additionally, boundary-based methods generally offer lower computational costs compared to grid-based methods and are especially advantageous for use with meshless aerodynamic solvers, where coupling to a grid-based CAA solver would defeat the dimension reduction achieved for the flow simulation step. Finally, most unsteady aerodynamic computations are performed in the time domain, leading to a natural coupling with time domain aeroacoustic methods. For these reasons, TDBEM formulations are especially promising for installed propeller noise prediction in combination with both mid-fidelity panel-VPM methods and other aerodynamic solvers.

In this work, we introduce a unified unsteady time domain approach to efficiently resolve tonal interaction noise, including aerodynamic installation effects from wake and potential interactions and acoustic installation effects from scattering and shielding. We couple an inviscid panel method with a viscous VPM wake model [23] for flow simulation to a Galerkin TDBEM [19] with forcing from the FWH aeroacoustic analogy to compute the far-field acoustic pressure. The approach is applied to study a propeller-wing configuration originally tested in a recent experimental campaign by Zawodny et al. (2021) [1]. The experimental measurements reported by Zawodny et al. are used to assess the proposed approach, and the numerical results are also used to analyze the significance of various physical mechanisms on the installation effects observed in the far-field acoustics.

II. Methodology

A. Aerodynamics

Aerodynamic simulations of the propeller-wing configuration are performed using the panel-VPM solver DUST [23]. DUST is an open-source computational fluid dynamics tool designed for efficient simulation of eVTOLs and other complex configurations. DUST uses an inviscid panel method with constant strength source-doublet panels to represent aircraft surfaces, solving for circulation over lifting bodies by enforcing the Kutta condition at the trailing edge. This approach requires a surface discretization for all aircraft elements, but removes the need for a more computationally expensive volume mesh.

DUST resolves the wake behind lifting surfaces with regularized Lagrangian vortex particles shed from each trailing edge panel. The stretching term is solved according to the transpose scheme, which has the advantage of explicitly conserving circulation [24]. Viscous diffusion in the wake is modeled with the particle strength exchange method [24]. The discrete nature of the vortex particle wake lends itself to stable solution of complicated wake-airframe interactions. While the vortex particles do not maintain core overlap through remeshing or other means, DUST does implement the divergence relaxation scheme of Pedrizzetti [25]. DUST includes compressibility effects at low subsonic Mach numbers via the Prandtl-Glauert correction. More details on the implementation of the mixed panel-VPM approach are provided by Montagnani et al. (2019)[26] and Tugnoli et al. (2021) [23].

Previous studies of aerodynamic interactions in installed propeller configurations using DUST have shown relatively good agreement in large-scale flow features compared to high-fidelity CFD and experiment [27, 28]. While this panel-VPM approach does not resolve incoherent wake structures or broadband noise sources, it may be able to capture coherent primary wake structures with sufficient accuracy to model important tonal installation effects.

B. Acoustics

The far-field acoustic pressure p' is computed via several substeps. First, at each timestep, the acoustic sources are extracted from the flow field and radiated to the far field in the absence of scattering effects according to the FWH Formulation 1A of Farassat [29] (hereafter referred to as the incident field denoted p'_i). The incident acoustic velocity on the solid surface geometry is evaluated with the V1A formulation of Ghorbaniasl et al. [30] from the same flow field quantities. The total acoustic pressure field is then computed as the sum of incident and scattered components, where the scattered pressure field p'_s is obtained by the TDBEM with the incident acoustic velocity as forcing to satisfy the acoustic boundary condition on the scattering surface.

Both F1A [29] and V1A [30] are formulated in terms of primitive variables of the flow, which are obtained from the panel-VPM. In keeping with the boundary discretization, we integrate the monopole and dipole distributions directly over the surface of the geometry and neglect the quadrupole terms in the volume integral. This approximation eliminates the need for careful selection of an integrating surface within the flow, and is often suitable for far-field noise estimation at low tip Mach numbers when contributions from quadrupole terms are expected to be minimal[31]. Both solvers implement a source time approach[32] in which acoustic pressure contributions are evaluated on the integrating surface at each emission timestep and are propagated to the observer time domain, where the full acoustic signal is constructed.

To account for the presence of non-compact solid bodies during the propagation step, we apply a recently developed spacetime Galerkin TDBEM [19]. From an incident acoustic field, the TDBEM computes a scattered field such that the total field satisfies the acoustic boundary condition on the scattering surface.

Assuming a uniform background flow, we apply the Prandtl-Glauert-Lorentz (PGL) transformation [33] to solve the scattering problem for the acoustic potential ϕ in the setting of the acoustic wave equation in a medium at rest:

$$\frac{1}{c_0^2}\frac{\partial^2 \phi}{\partial t^2} - \frac{\partial^2 \phi}{\partial x_i^2} = s\left(\boldsymbol{x}, t\right), \tag{1}$$

where s is the transformed acoustic source distribution, c_0 is the speed of sound, and $\boldsymbol{x}$ and t denote the spatial and temporal coordinates in the transformed variables. Other classes of background flows can be considered using different variable transformations, such as the low Mach number approximation due to Taylor [34], and the weakly nonuniform approximation of Mancini et al. [35]. In this work, the uniform background flow approximation is applied because it matches the propagation assumptions of the moving observer FWH formulation without the quadrupole term.

We apply the sound-hard boundary condition, which is equivalent to requiring zero normal acoustic velocity (acoustic potential gradient) in the transformed coordinates, or zero energy flux in physical coordinates [33]. The normal

gradient on the boundary due to the incident contribution is:

$$\frac{\partial \phi_i}{\partial n_{\boldsymbol{x}}}(\boldsymbol{x}, t) = \int \frac{\partial G}{\partial n_{\boldsymbol{x}}} s(\boldsymbol{y}, \tau)\, d\boldsymbol{y} d\tau = -g(\boldsymbol{x}, t), \tag{2}$$

where $\frac{\partial}{\partial n}$ denotes the gradient in the normal direction, $\boldsymbol{x}$ and t are the observer space and time variables, $\boldsymbol{y}$ and τ are emission space and time variables, and $G(\boldsymbol{x}, \boldsymbol{y}, t, \tau)$ is the free-space Green's function for the acoustic wave equation:

$$G(\boldsymbol{x}, \boldsymbol{y}, t, \tau) = \frac{\delta\left(t - \tau - \frac{|\boldsymbol{x}-\boldsymbol{y}|}{c_0}\right)}{4\pi|\boldsymbol{x}-\boldsymbol{y}|}. \tag{3}$$

To obtain a total field that satisfies the boundary condition, the scattered field must be a homogeneous solution of (1) (i.e., with $s(\boldsymbol{x}, t) = 0$) with the Neumann boundary condition:

$$\frac{\partial \phi_s}{\partial n_{\boldsymbol{x}}}(\boldsymbol{x}, t) = g(\boldsymbol{x}, t) \text{ on } \Gamma, \tag{4}$$

where Γ is the scattering surface.

The TDBEM computes the scattered component based on the first kind spacetime-conforming Galerkin formulation of Ha-Duong [36]. The boundary element approach represents the scattered field with surface distributions of the double layer potential, which corresponds to the jump in acoustic potential over the boundary $\psi = \left[\frac{\partial \phi_s}{\partial n}\right]$. The first kind boundary integral equation for the double layer potential is:

$$g(\boldsymbol{x}, t) = \frac{\partial \phi_s}{\partial n_{\boldsymbol{x}}}(\boldsymbol{x}, t) = \int_0^t \int_\Gamma \frac{\partial^2 G}{\partial n_{\boldsymbol{x}} \partial n_{\boldsymbol{y}}} \psi(\boldsymbol{y}, \tau)\, d\boldsymbol{y} d\tau, \tag{5}$$

for $\boldsymbol{x} \in \Gamma$, $t \in [0, T]$, with initial condition $\phi_s(\boldsymbol{x}, 0) = 0$. Bamberger and Ha-Duong [37] show that the appropriate weak form of (5) for full Galerkin discretization is:

$$a(\psi, \eta) := \int_0^T \int_\Gamma \dot{\eta}(\boldsymbol{x}, t) \int_\Gamma \frac{\partial^2 G}{\partial n_{\boldsymbol{x}} \partial n_{\boldsymbol{y}}} \psi(\boldsymbol{y}, \tau)\, d\boldsymbol{y} d\boldsymbol{x} dt = f(\eta) := \int_0^T \int_\Gamma \dot{\eta}(\boldsymbol{x}, t)\, g(\boldsymbol{x}, t)\, d\boldsymbol{x} dt, \tag{6}$$

for all test functions η belonging to the same space as the trial functions, where $\dot{\eta}$ denotes the time derivative. The weak form is discretized with piecewise linear test and trial basis elements in space and time on a triangular surface mesh.

After evaluating the scattered acoustic potential in transformed coordinates, the scattered pressure can be recovered as:

$$p_s' = -\rho_\infty \left(\frac{\partial \phi_s}{\partial T} + U_i \frac{\partial \phi_s}{\partial X_i}\right), \tag{7}$$

where ρ_∞ is the ambient density, $\boldsymbol{U}$ is the uniform background flow velocity, and $\boldsymbol{X}$ and T are the spatial and temporal coordinates in the physical variables.

The spacetime Galerkin formulation is notable for being unconditionally stable [36, 37]. It also has a number of numerical and practical advantages over alternative TDBEM schemes, such as Burton-Miller reformulation with point collocation [38]. Galerkin approaches avoid the introduction of additional numerical parameters that must be tuned, as is the case in Burton-Miller reformulation, where a coupling parameter must be chosen carefully to obtain accurate results [39]. The double spatial integration required by the full Galerkin approach gives greater flexibility because it allows simulation of open scattering surfaces and coincident source-scatterer surfaces, which result in hypersingular integrands in the collocation approach. Finally, Galerkin methods benefit from a quasi-best approximation property in the energy norm that tends to result in more accurate solutions with a given discretization compared to collocation methods [40], which may be particularly beneficial given the high asymptotic cost scaling of integral methods.

III. Propeller-Wing Configuration and Experimental Results

In this paper, the panel-VPM-TDBEM approach is applied to a tractor propeller-wing configuration tested by Zawodny et al. (2021) [1].

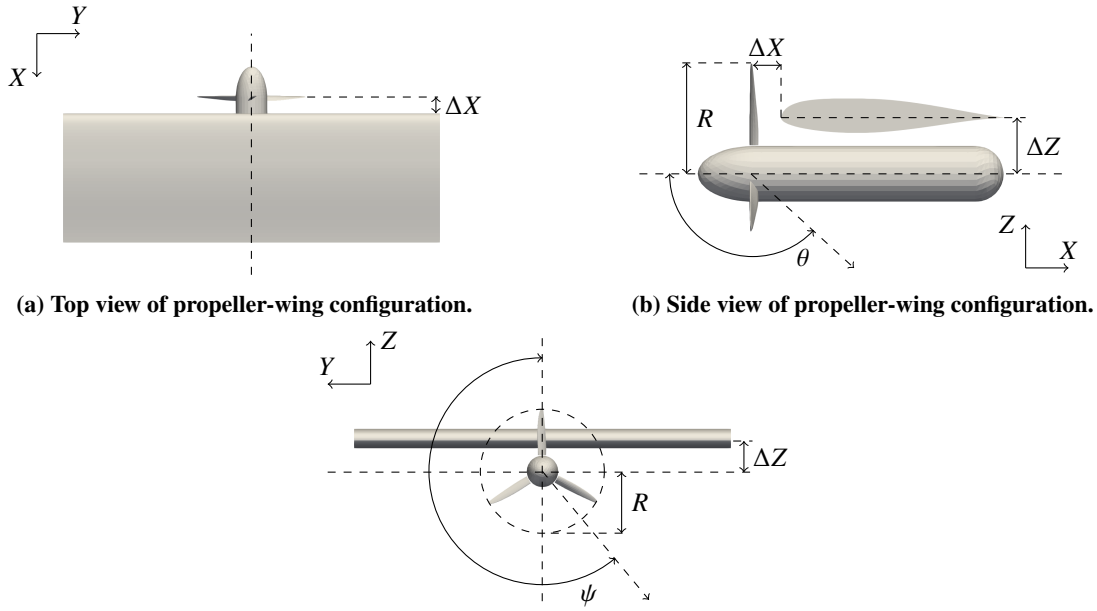

(a) Top view of propeller-wing configuration.

(b) Side view of propeller-wing configuration.

(c) Front view of propeller-wing configuration.

Fig. 1 Propeller-wing geometry, consisting of a three-bladed propeller installed on a nacelle below a rectangular wing. The wing leading edge is located at $(\Delta X, 0, \Delta Z)$ relative to the center of the propeller disk. The flyover observer array is located 3.5 m from the propeller axis at an azimuthal angle $\psi = 220°$.

A. Experimental Measurements

The experiments were conducted by Zawodny et al. [1] in the Low Speed Aeroacoustic Wind Tunnel (LSAWT) facility at the NASA Langley Research Center. This facility is an open-circuit, open-jet anechoic wind tunnel, with a cut-off frequency of 250 Hz. The test section was outfitted with a linear array of 28 6.35 mm-diameter B&K model 4939 microphones, located 3.5 m from the propeller axis at an azimuthal angle of 220° below the configuration. Propeller thrust and torque were measured with an ATI-IA Mini45 load cell. Steady and unsteady pressures were measured at several chordwise and spanwise positions on the wing using pressure taps and a 3.2 mm thick sleeve containing a row of Kulite LQ-064 sensors.

The propeller-wing configuration consisted of a three-bladed Mejzlik 16x11 propeller with a diameter of 0.2 m. The propeller was installed on a nacelle located below the midspan of a NACA 63_2-215 MOD B wing with 0.406 m chord and 2.44 m span. The wing was mounted on a traverse and was positioned at several vertical and axial separations relative to the propeller. In particular, experimental data are available for axial separations $\frac{\Delta X}{R} \in [0.25, 1.5]$ and vertical separations $\frac{\Delta Z}{R} \in [0.5, 2]$. Measurements were collected at a constant propeller rotational speed of $\Omega = 6000$ rpm at an advance ratio of $J = 0.592$. The reported acoustic data focus on the first blade passage frequency (BPF) due to motor noise contamination at higher harmonics.

B. Numerical Setup

The propeller-wing configuration geometry in DUST is shown in Figure 1. Two modifications are made compared to the experimental setup. First, a notional nacelle geometry is used as the tested hub and nacelle geometries were not available. Second, the span of the wing is decreased to 1.2 m to reduce the computational cost while retaining the portion of the wing responsible for installation effects. Several propeller discretizations, ranging from 1392 to 4176 panels, are considered to determine the sensitivity to spatial resolution. The wing and nacelle discretizations are not varied but are very highly resolved, with 5580 and 1242 panels, respectively. The wing includes a spanwise refinement region out to 1.5R on each side of the centerline. The timestep is also varied from 3-9° blade azimuth per step to determine temporal resolution requirements. Simulations are run for ten total revolutions, and aerodynamic and acoustic data are collected over the last five revolutions after the simulations have stabilized.

The scattering analysis focuses on the wing as the primary scattering body. Separate acoustic surface discretizations

are used because the requirements for a high-quality acoustic surface mesh are different from the surface panel discretization. In particular, the acoustic discretization prioritizes uniformly sized nearly isotropic meshes in the transformed PGL coordinates. To assess spatial resolution requirements, two different surface discretizations are considered with 1384 and 2500 elements. Because of difficulties interpolating between separately generated aerodynamic and acoustic discretizations, the scattering analysis uses forcing from the blade and nacelle but neglects the self-scattering of sources on the wing. This mechanism will be considered in future work.

IV. Aerodynamic Analysis

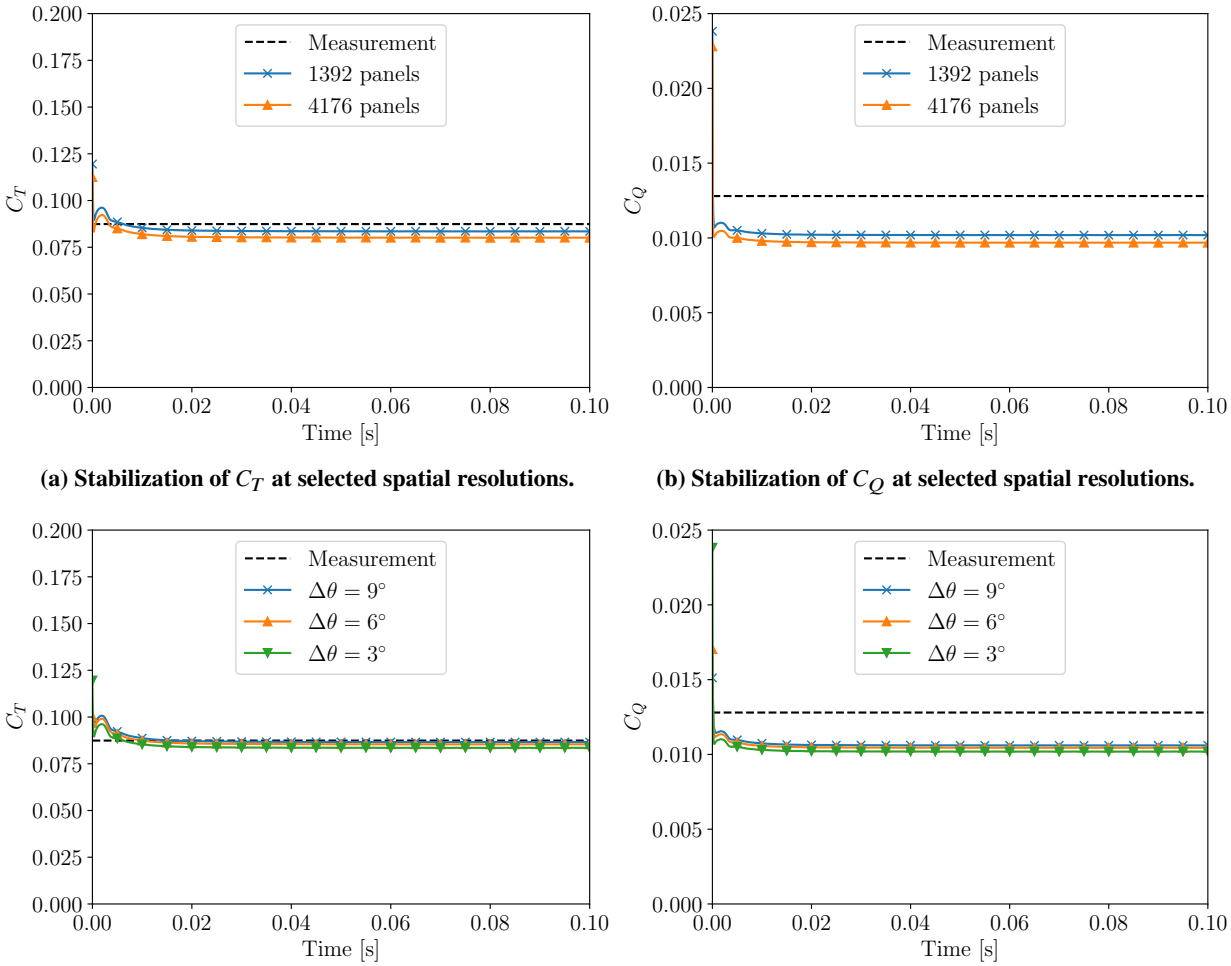

(a) Stabilization of C_T at selected spatial resolutions.

(b) Stabilization of C_Q at selected spatial resolutions.

(c) Stabilization of C_T at selected temporal resolutions.

(d) Stabilization of C_Q at selected temporal resolutions.

Fig. 2 Stabilization of isolated propeller thrust and torque coefficients compared with experimental measurement. Thrust is consistently well predicted, while the torque is underpredicted. The sensitivity to spatial and temporal resolution is small.

To assess the accuracy of the DUST simulation and determine resolution sensitivities, aerodynamic results are compared against the reported experimental measurements. Figure 2 compares the isolated propeller thrust and torque coefficients over the ten simulated revolutions. Both coefficients stabilize rapidly within the first three revolutions, and display little sensitivity to either spatial or temporal resolution. While the thrust coefficients track closely with experiment, the torque is significantly underpredicted. This is expected because viscous stresses are not captured by the inviscid panel formulation.

Figures 3 and 4 compare nondimensionalized root mean square fluctuating pressures $C'_{p,RMS}$ on the wing in the

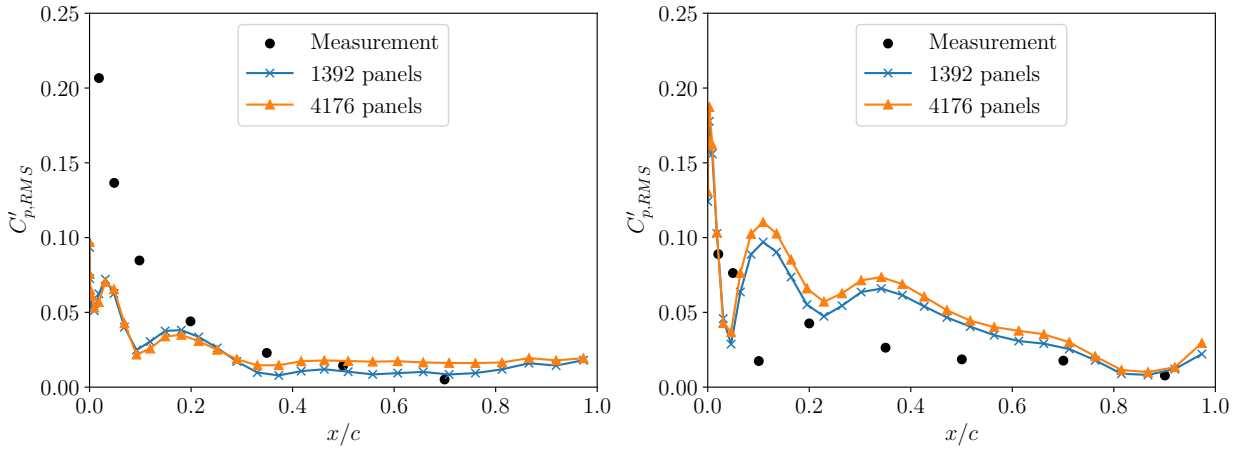

(a) Suction side $C'_{p,RMS}$ at selected spatial resolutions.

(b) Pressure side $C'_{p,RMS}$ at selected spatial resolutions.

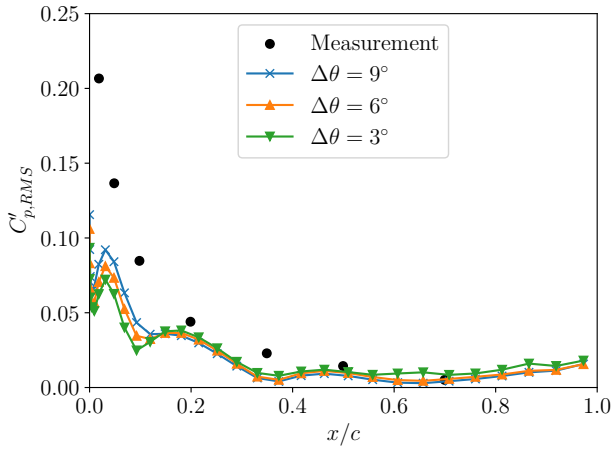

(c) Suction side $C'_{p,RMS}$ at selected temporal resolutions.

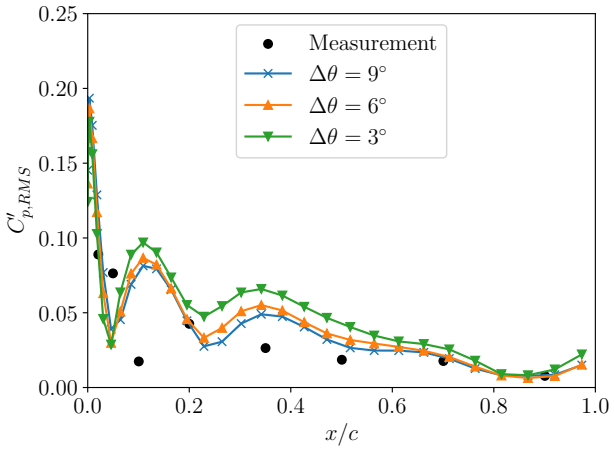

(d) Pressure side $C'_{p,RMS}$ at selected temporal resolutions.

Fig. 3 Chordwise distributions of $C'_{p,RMS}$ along the wing centerline ($\frac{\Delta X}{R} = 0.25$, $\frac{\Delta Z}{R} = 0.5$). The sensitivity to spatial and temporal resolution is small.

$\frac{\Delta X}{R} = 0.25$, $\frac{\Delta Z}{R} = 0.5$ position. Figure 3 shows chordwise slices along the centerline on the suction and pressure sides. The suction side shows substantial underprediction at the leading edge and better agreement downstream, while the pressure side shows decent agreement over the chord. The sensitivity to both propeller spatial resolution and temporal resolution is relatively small. Figure 4 shows chordwise slices near the tip vortex path at $Y = -0.866$R. Here, substantial deviations from experiment are observed on both the suction and pressure sides. The leading edge shows decent agreement on both sides, while the fluctuations are significantly overpredicted downstream of the leading edge. This may be due to the inviscid slip wall boundary condition and the absence of a boundary layer, which allows vortical strucures to stretch and intensify near the wall without the damping effect of the viscous shear layer, causing unphysically large pressure fluctuations behind the leading edge. The distributions show little sensitivity to propeller spatial resolution but significant sensitivity to increased temporal resolution.

The aerodynamic comparison raises questions about the accuracy of the pressure fluctuations caused by the tip vortex impingement as captured by DUST. While the resolution study is not exhaustive and, in particular, does not include the effects of varying wing spatial resolution, the overall resolution in both space and time is relatively high for a mid-fidelity simulation. These discrepancies may represent a broader limitation of mid-fidelity aerodynamic solvers that do not capture viscous near-wall effects for propeller-wing interaction problems. A comparison with a boundary layer-resolving aerodynamic solver would be useful to assess whether this limitation substantially limits the noise prediction capabilities.

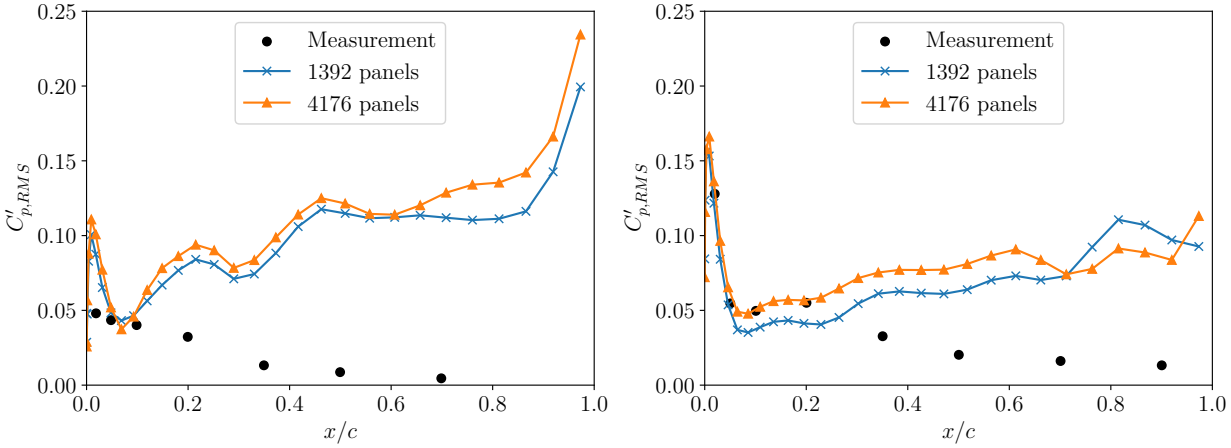

(a) Suction side $C'_{p,RMS}$ at selected spatial resolutions.

(b) Pressure side $C'_{p,RMS}$ at selected spatial resolutions.

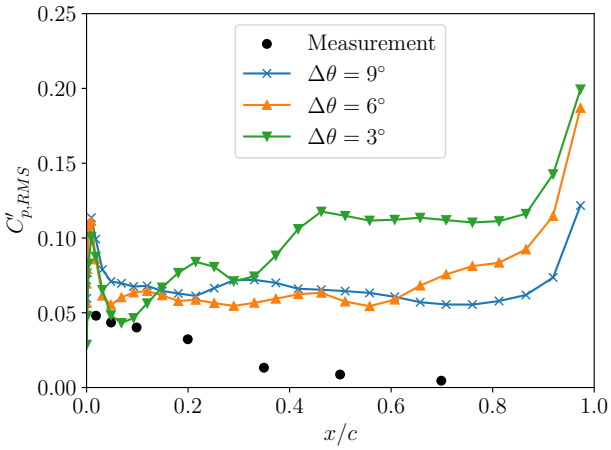

(c) Suction side $C'_{p,RMS}$ at selected temporal resolutions.

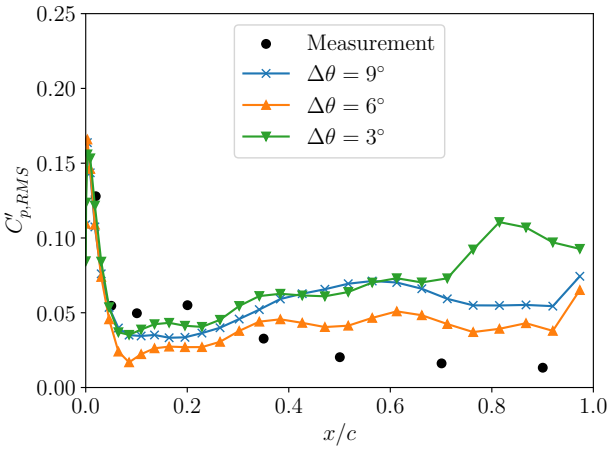

(d) Pressure side $C'_{p,RMS}$ at selected temporal resolutions.

Fig. 4 Chordwise distributions of $C'_{p,RMS}$ near the tip vortex path ($Y = -0.866\mathbf{R}$) on the wing ($\frac{\Delta X}{R} = 0.25$, $\frac{\Delta Z}{R} = 0.5$). The sensitivity to spatial resolution is small, while reducing the timestep results in a substantial increase in fluctuations on both suction and pressure sides.

V. Acoustic Analysis

Due to the availability of experimental measurements, the acoustic analysis focuses on the first BPF. Far-field acoustic predictions are compared for across varying spatial and temporal resolutions to determine resolution requirements. Figure 5 compares sound pressure level (SPL) flyover directivity at varying propeller spatial resolution and temporal resolution for both the isolated propeller (propeller and nacelle only, with no wing present in aerodynamic or acoustic computations) and the installed configuration with wing location $\frac{\Delta X}{R} = 0.25$, $\frac{\Delta Z}{R} = 0.5$. The installed propeller directivity is plotted without the scattered component (incident component p_i only) to highlight the resolution effects on the noise sources. The isolated propeller directivity shows no sensitivity to temporal or spatial refinement. The installed propeller directivity shows minimal sensitivity to spatial refinement except around $\theta = 135°$, where a finer propeller discretization leads to a more pronounced drop in the SPL. Changes in temporal resolution result in moderate changes in SPL at most flyover angles. On the basis of these acoustic results, together with the aerodynamic comparisons presented in Section IV, a coarser propeller spatial resolution of 1392 panels combined with the smallest 3° timestep seems to provide the best compromise of accuracy and cost. Subsequent results are obtained using this combination of propeller spatial resolution and temporal resolution.

The spatial resolution sensitivity of the TDBEM scattering computation is also considered. The directivity of the scattered contribution p_s with two acoustic meshes is shown in Figure 6. While the directivities are qualitatively similar,

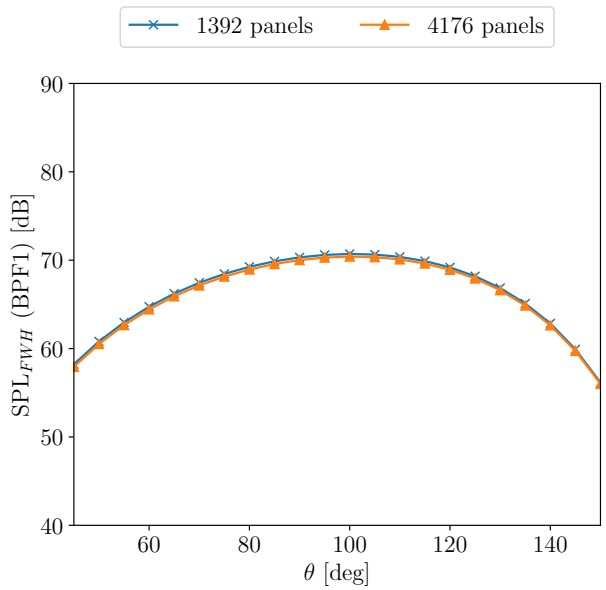

(a) Isolated propeller SPL at selected spatial resolutions.

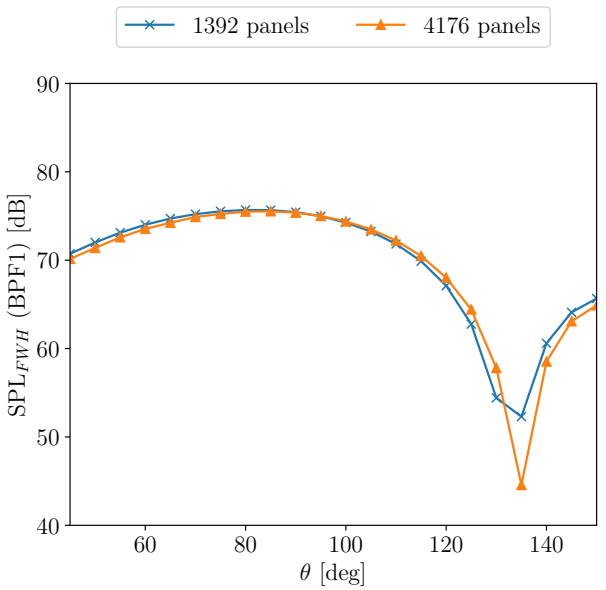

(b) Installed propeller SPL (without scattering) at selected spatial resolutions.

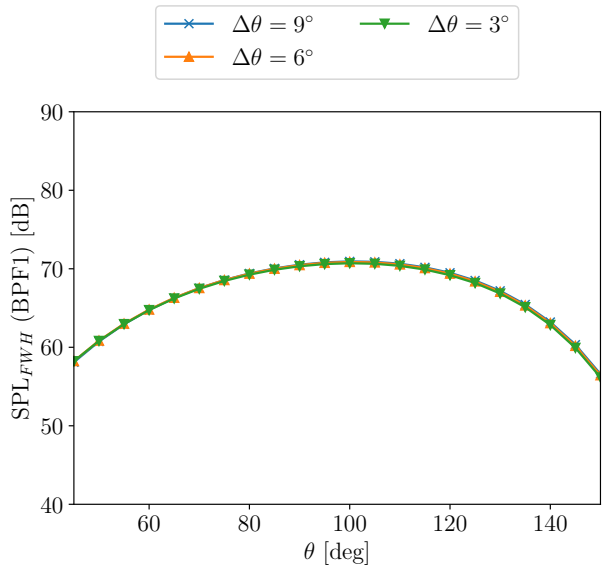

(c) Isolated propeller SPL at selected temporal resolutions.

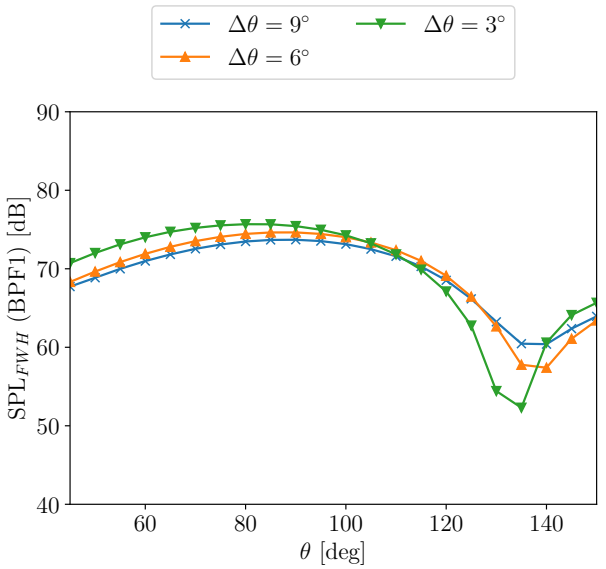

(d) Installed propeller SPL (without scattering) at selected temporal resolutions.

Fig. 5 Comparison of isolated and installed flyover directivities at different spatial and temporal resolutions.

the level is reduced by up to five dB for the larger mesh. Future work will compare a larger hierarchy of acoustic meshes to obtain full convergence of the scattered contribution. For subsequent results, the higher resolution mesh with 2500 surface elements is used.

The installed propeller flyover SPL directivity is compared against experimental measurements to assess the accuracy of the panel-VPM-TDBEM approach. Two sweeps of wing positions are considered: a vertical sweep with constant $\Delta X/R = 0.25$ at $\Delta Z/R = 0.5, 0.75, 1.0, 1.5$, and an axial sweep with constant $\Delta Z/R = 0.5$ at $\Delta X/R = 0.25, 0.5, 1.0, 1.5$. The simulated and measured installed propeller directivities are compared in Figures 7 and 8 for the vertical and axial position sweeps, respectively. The isolated propeller simulation and measurement is included for comparison.

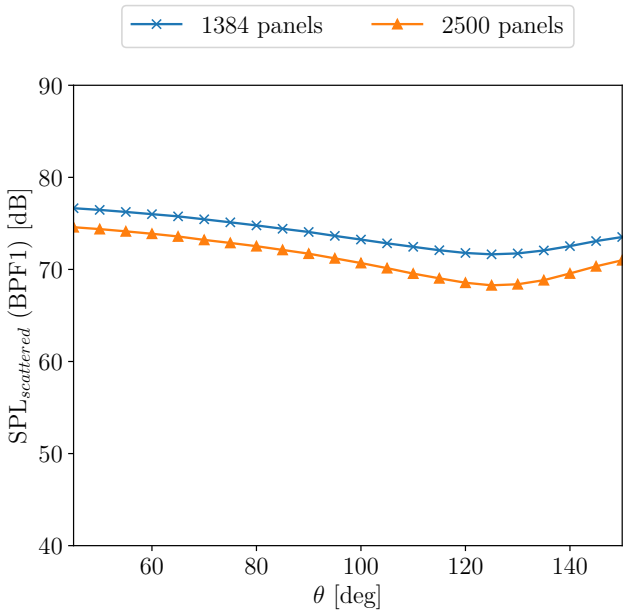

Fig. 6 Comparison of scattered contribution at different acoustic surface mesh spatial resolutions. The wing location $\frac{\Delta X}{R} = 0.25$, $\frac{\Delta Z}{R} = 0.5$ is shown for $\Delta\theta = 3°$ and 1392 blade panels.

Overall, many key qualitative features of the installed configuration directivities are captured, but significant discrepancies also remain. At the nearest wing location ($\frac{\Delta X}{R} = 0.25$, $\frac{\Delta Z}{R} = 0.5$), the amplification at low and high flyover angles is captured, with good agreement near $\theta = 45°$ and $\theta = 150°$. The intermediate angles are underpredicted relative to the experiment, although qualitative features such as the dip at $\theta = 100°$ and the peak at $\theta = 130°$ are captured. At $\frac{\Delta X}{R} = 0.25$, $\frac{\Delta Z}{R} = 0.75$, the low and high flyover angles are again accurately captured, but a very significant discrepancy exists in the intermediate angles, where a substantial decrease in the in-plane levels is not captured. At $\frac{\Delta X}{R} = 0.25$, $\frac{\Delta Z}{R} = 1.0$, the qualitative shape of the directivity is captured, including a slight dip in the propeller plane, but the levels are overpredicted relative to the measurement, particularly around $\theta = 45°$ and $\theta = 120°$. At the largest vertical separation ($\frac{\Delta X}{R} = 0.25$, $\frac{\Delta Z}{R} = 1.5$), the simulated installation effects are very small. A slight amplification near $\theta = 140°$ over the isolated case is captured at a level comparable to the experiment, but the measured amplification from $\theta = 45°$ to $\theta = 90°$ is not observed. At $\frac{\Delta X}{R} = 0.5$, $\frac{\Delta Z}{R} = 0.5$, the simulation captures amplification around $\theta = 45°$ but the dip in the measured directivity near $\theta = 80°$ is instead shifted forward to $\theta = 60°$, resulting in significant underprediction at this location. The agreement is good in the propeller plane and at $\theta = 150°$, but a second dip is observed around $\theta = 140°$ that is missing from the measured directivity, leading to significant underprediction. At $\frac{\Delta X}{R} = 1.0$, $\frac{\Delta Z}{R} = 0.5$, the simulated and measured directivities are qualitatively very similar, with a consistent offset of around five dB. Both directivities show higher levels around $\theta = 45°$ and reduced levels around $\theta = 120°$. Finally, at the largest axial separation ($\frac{\Delta X}{R} = 1.5$, $\frac{\Delta Z}{R} = 0.5$), minimal installation effects are observed in the simulated directivity, resulting in significant underprediction at forward angles and overprediction around $\theta = 130°$.

To identify the physical mechanisms in the simulated results, differences between selected acoustic contributions are plotted for the vertical and axial wing location sweeps in Figures 9 and 10, respectively. In particular, three important interaction mechanisms, propeller potential interaction, wake impingement, and acoustic scattering, are investigated by comparing the difference between the installed and isolated propeller blade contribution ($\mathrm{SPL}_{pw,blade} - \mathrm{SPL}_{p,blade}$), the difference between the total SPL with and without the wing contribution ($\mathrm{SPL}_{total} - \mathrm{SPL}_{no\,wing}$), and the difference between the total SPL with and without the scattered contribution ($\mathrm{SPL}_{total} - \mathrm{SPL}_{incident}$), respectively. These interaction mechanisms are not exhaustive, but they are hypothesized to be among the most significant in installed propeller configurations [1].

The blade installation comparison ($\mathrm{SPL}_{pw,blade} - \mathrm{SPL}_{p,blade}$) shows significant differences of over 10 dB at low and high flyover angles, with minimal effect in the propeller plane. The differences are observed to decrease very rapidly with increasing vertical and axial separation. This comparison is expected to be dominated by the propeller interaction with the potential flow around the wing leading edge that drives changes in the local blade angle of attack as it passes

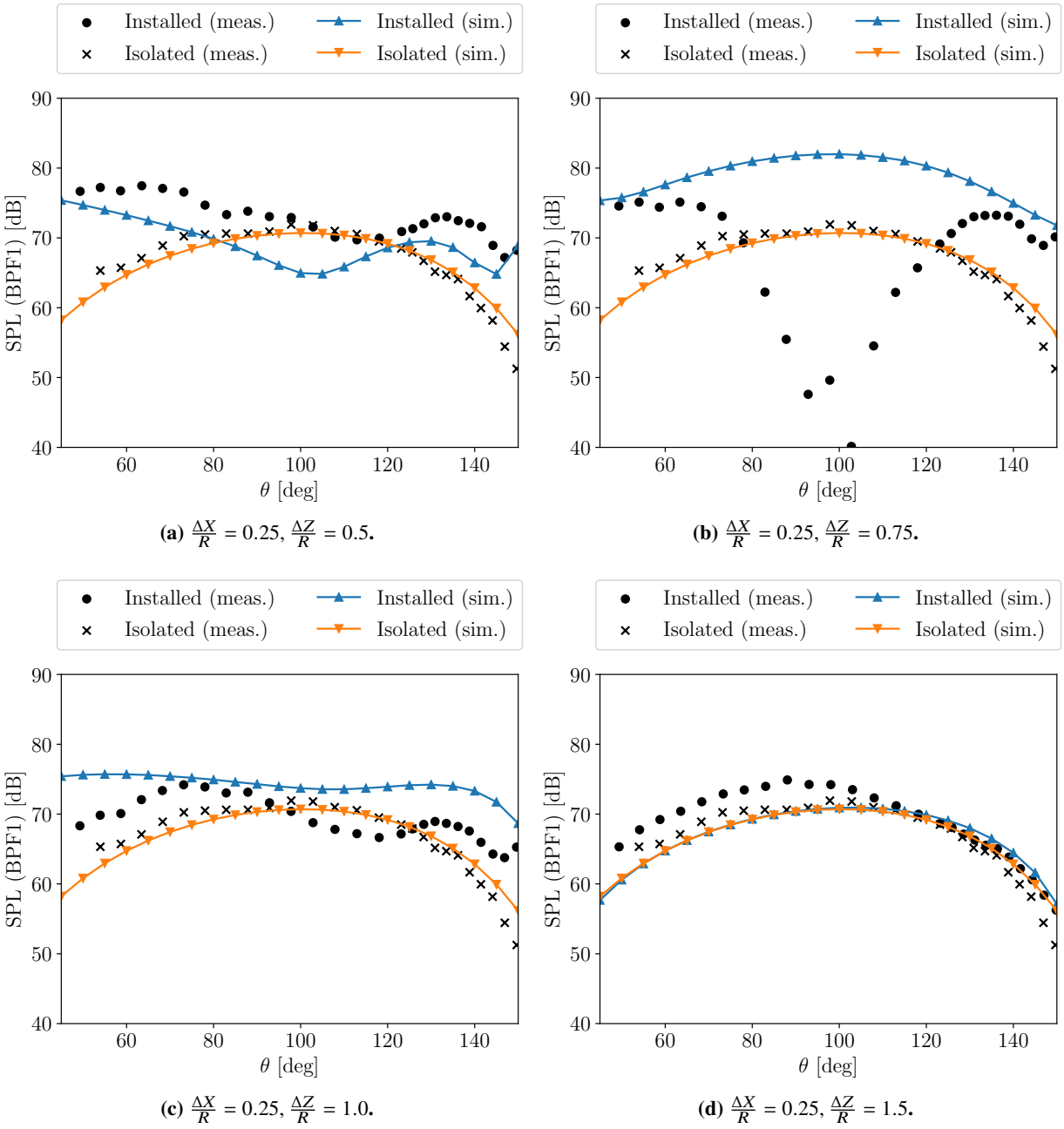

(a) $\frac{\Delta X}{R} = 0.25$, $\frac{\Delta Z}{R} = 0.5$.

(b) $\frac{\Delta X}{R} = 0.25$, $\frac{\Delta Z}{R} = 0.75$.

(c) $\frac{\Delta X}{R} = 0.25$, $\frac{\Delta Z}{R} = 1.0$.

(d) $\frac{\Delta X}{R} = 0.25$, $\frac{\Delta Z}{R} = 1.5$.

Fig. 7 Comparison of measured and simulated installed propeller flyover SPL directivities at varying vertical wing locations. The measured and simulated isolated propeller directivities are also included for reference.

near the wing. The observed trends are well-explained by this mechanism. In particular, it primarily affects the blade loading, leading to the observed forward and backward directivity effects, and it decreases rapidly as the wing leading edge is moved away from the propeller disk.

The wing contribution comparison ($\text{SPL}_{total} - \text{SPL}_{no\,wing}$) shows significant differences above 15 dB, primarily around $\theta = 120°$ for the closest wing locations, with reduced differences at forward and backward directivities. The effect decreases rapidly with increasing vertical separation, while it decreases more slowly with axial separation. This contribution is expected to be dominated by the wake impingement effect on the wing. This explanation also aligns well with the observed trends. In particular, the effect decreases more slowly with axial separation when the wing remains in

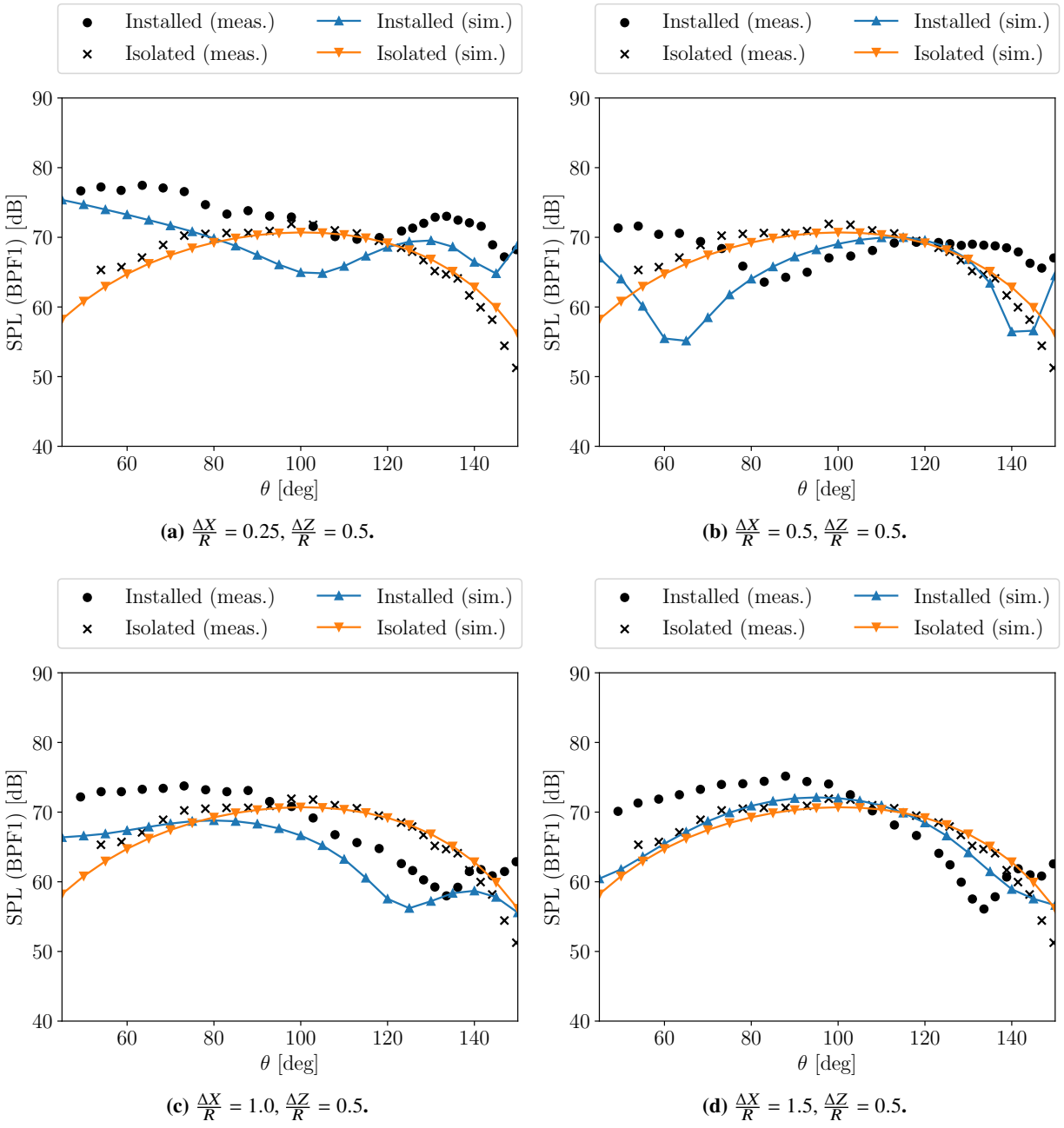

(a) $\frac{\Delta X}{R} = 0.25$, $\frac{\Delta Z}{R} = 0.5$.

(b) $\frac{\Delta X}{R} = 0.5$, $\frac{\Delta Z}{R} = 0.5$.

(c) $\frac{\Delta X}{R} = 1.0$, $\frac{\Delta Z}{R} = 0.5$.

(d) $\frac{\Delta X}{R} = 1.5$, $\frac{\Delta Z}{R} = 0.5$.

Fig. 8 Comparison of measured and simulated installed propeller flyover SPL directivities at varying axial wing locations. The measured and simulated isolated propeller directivities are also included for reference.

the propeller slip-stream than with vertical separation when the wing moves above it.

The scattered contribution comparison ($\text{SPL}_{total} - \text{SPL}_{incident}$) shows comparable magnitudes of over 15 dB. This comparison directly corresponds to the scattering of the acoustic fields radiated by the propeller and nacelle off the wing. Unlike the other two comparisons, the scattering effect is significant at all directivities, depending on the wing position, and does not noticeably decrease until vertical or axial separations are above one propeller radius. These trends are explained by the characteristics of the near-field acoustic pressure distribution around the propeller. Figures 11 and 12 show the phase of the propeller acoustic field on selected horizontal, meridional, and azimuthal slices, revealing the spatial structure of the incident acoustic field at key locations. The propeller is not a compact noise source and

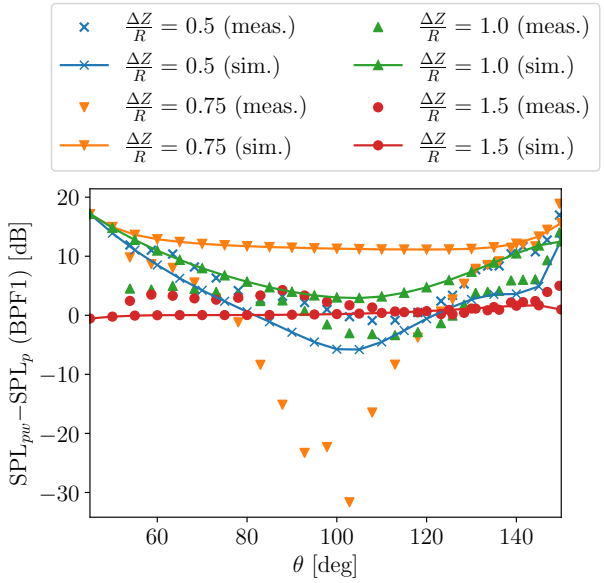

(a) Total installation effect.

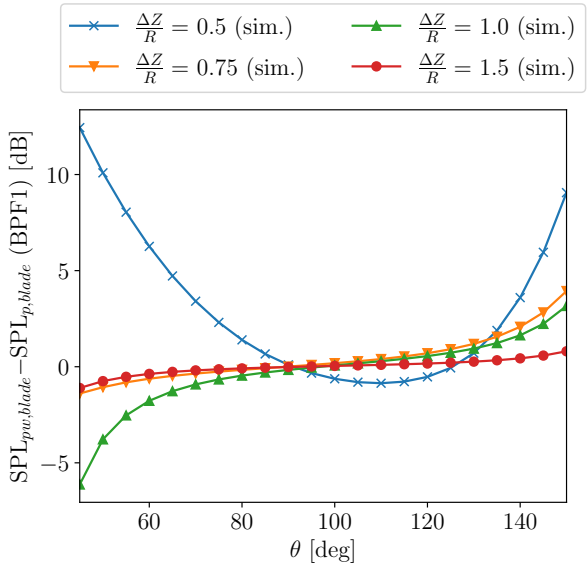

(b) Blade installation effect.

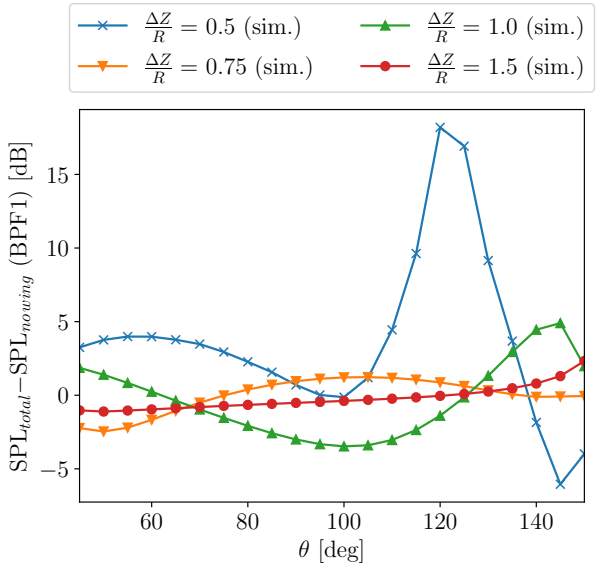

(c) Wing contribution.

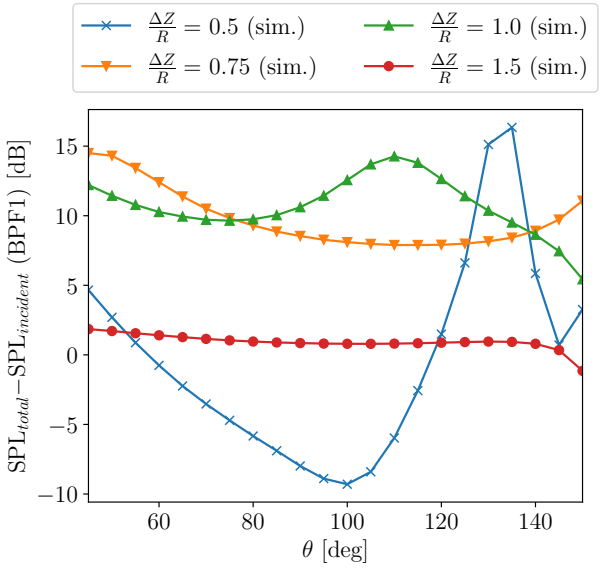

(d) Scattering contribution.

Fig. 9 Breakdown of installation effects for the vertical wing location sweep: (a) total installation effect compared against experiment; (b) difference between installed and isolated blade contributions, indicative of the propeller potential interaction mechanism; (c) difference between installed directivities with and without the wing contribution, indicative of the wake impingement interaction mechanism; (d) difference between installed directivities with and without the scattered contribution, corresponding to the scattering acoustic interaction mechanism.

is therefore characterized by different length scales in the near field and far field. In the far field, the acoustic length scale is the wavelength, which is on the order of the wing span and far larger than the wing chord, resulting in weak incident gradients and minimal scattering. The near-field length scale is determined by the propeller diameter, which is over an order of magnitude smaller than the wavelength. Therefore, while the scattering surface is acoustically compact with respect to the far-field length scale, it is not compact with respect to the near field, resulting in significant

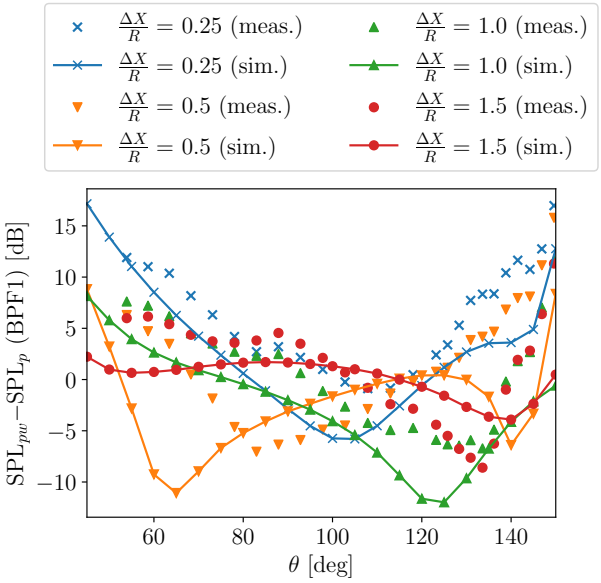

(a) Total installation effect.

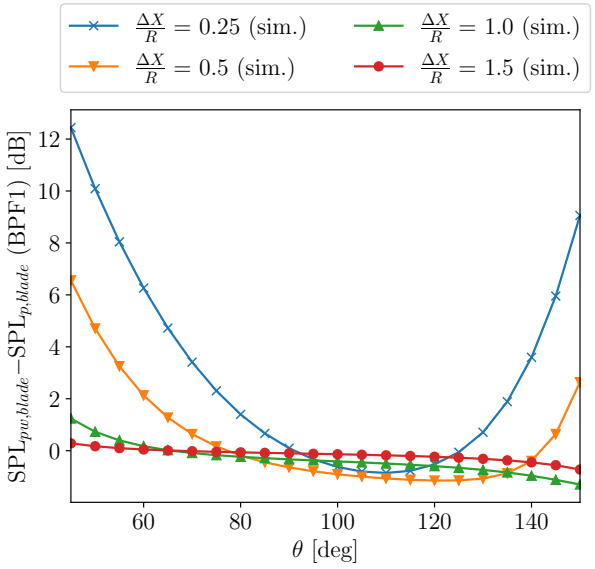

(b) Blade installation effect.

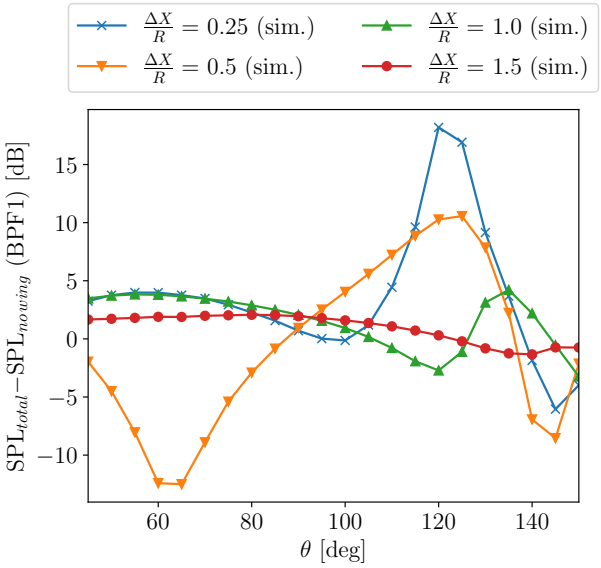

(c) Wing contribution.

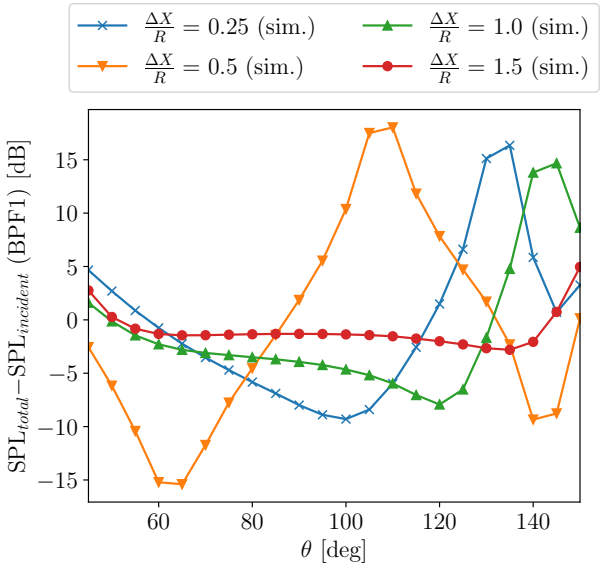

(d) Scattering contribution.

Fig. 10 Breakdown of installation effects for the axial wing location sweep: (a) total installation effect compared against experiment; (b) difference between installed and isolated blade contributions, indicative of the propeller potential interaction mechanism; (c) difference between installed directivities with and without the wing contribution, indicative of the wake impingement interaction mechanism; (d) difference between installed directivities with and without the scattered contribution, corresponding to the scattering acoustic interaction mechanism.

scattering effects for wing positions near the propeller disk. The azimuthal and meridian slices show a near field that extends around one propeller radius in front and behind the propeller disk. Above the propeller disk and more than one radius in front or behind the disk there is a transition region, with length scales that fall in between the near-field scale and the wavelength. Finally, the far-field length scaling is mostly recovered starting about four radii from the propeller. The difference between the immediate near field and the transition scaling is especially apparent comparing

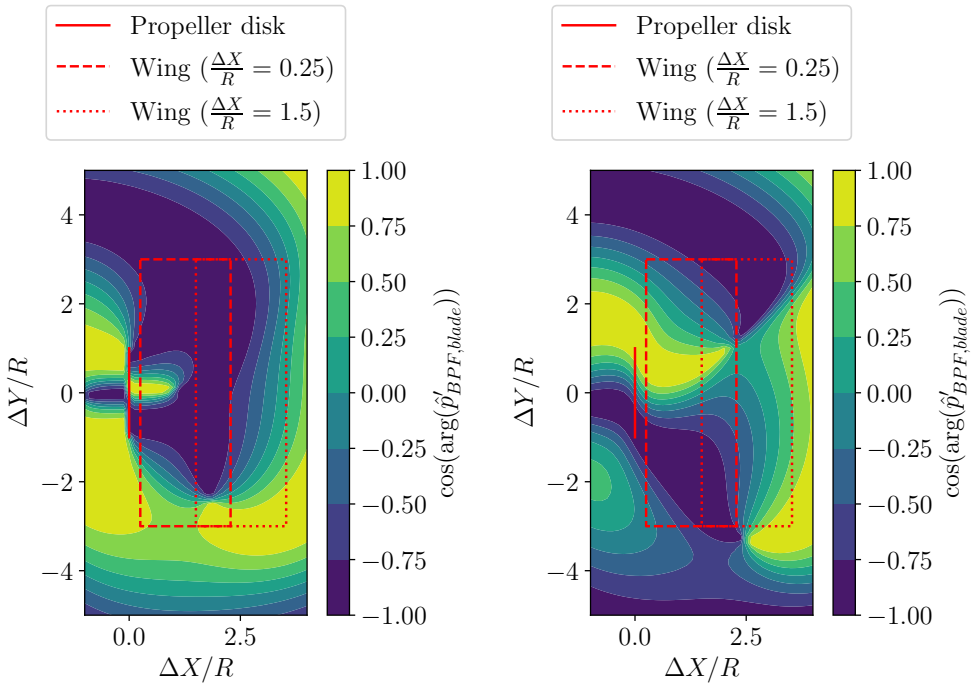

(a) Horizontal plane $\frac{\Delta Z}{R} = 0.5$.

(b) Horizontal plane $\frac{\Delta Z}{R} = 1.5$.

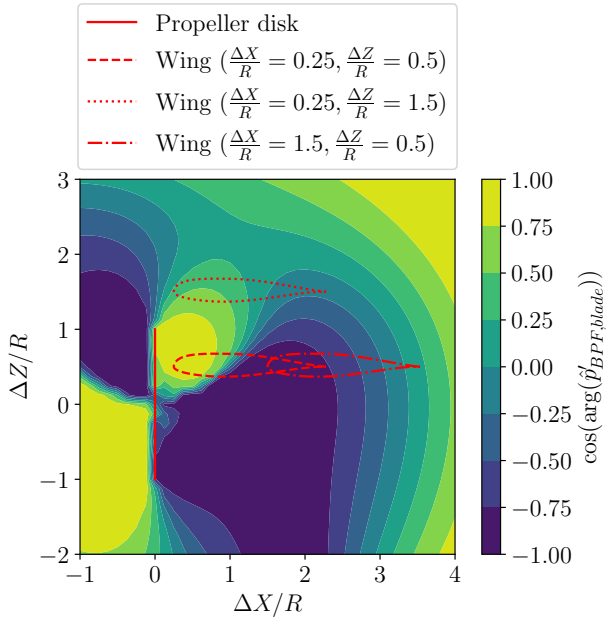

(c) Meridian plane.

Fig. 11 The cosine of the phase angle of the propeller incident acoustic contribution is plotted on horizontal and meridian planes to visualize the spatial structure: (a) horizontal plane at $\frac{\Delta Z}{R} = 0.5$, corresponding to the wing plane at the smallest vertical separation; (b) horizontal plane at $\frac{\Delta Z}{R} = 1.5$, corresponding to the wing plane at the largest vertical separation; (c) the meridian plane on the centerline. The propeller incident contribution from the $\frac{\Delta X}{R} = 0.25$, $\frac{\Delta Z}{R} = 0.5$ wing location is shown, although the structure of the acoustic field is illustrative of all the installed and isolated cases.

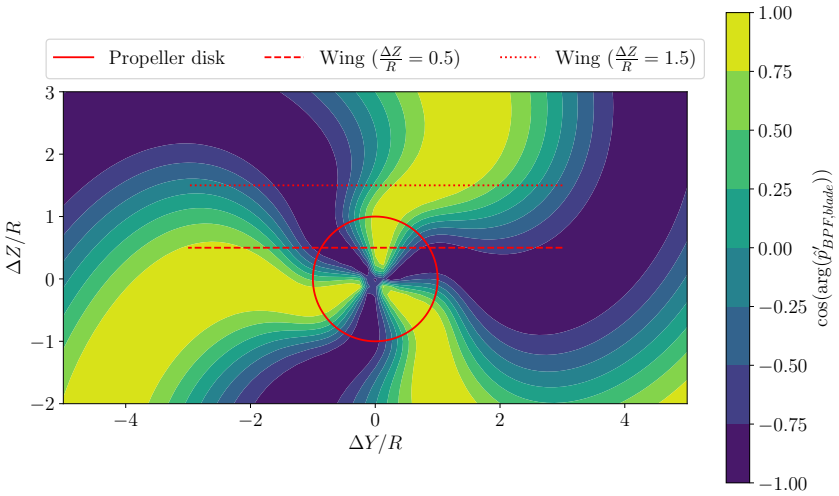

(a) Azimuthal plane $\frac{\Delta X}{R} = 0.25$.

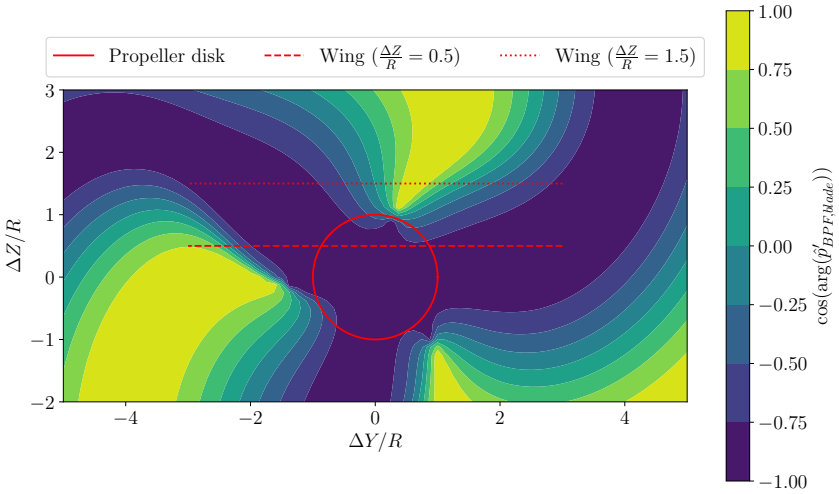

(b) Azimuthal plane $\frac{\Delta X}{R} = 1.5$.

Fig. 12 The cosine of the phase angle of the propeller incident acoustic contribution is plotted on azimuthal planes to visualize the spatial structure: (a) azimuthal plane at $\frac{\Delta X}{R} = 0.25$, corresponding to the wing leading edge at the smallest axial separation; (b) azimuthal plane at $\frac{\Delta X}{R} = 1.5$, corresponding to the wing leading edge at the largest axial separation. The propeller incident contribution from the $\frac{\Delta X}{R} = 0.25$, $\frac{\Delta Z}{R} = 0.5$ wing location is shown, although the structure of the acoustic field is illustrative of all the installed and isolated cases.

the azimuthal slices in the region behind the propeller disk and the two wing positions in the $\frac{\Delta X}{R} = 0.25$ slice. The nearest three positions in both the vertical and axial location sweeps have substantial portions of the wing leading edge in the propeller near field, and show scattered contributions of up to 15 dB. The farthest positions in both sweeps are located in the transition region, resulting in significantly less scattering.

Overall, all three interaction mechanisms are found to be significant across the selected wing positions. At the nearest wing positions, all three have similar contribution magnitudes. The total installation effect in these positions (roughly $\frac{\Delta X}{R} \in [0.25, 0.5]$, $\frac{\Delta Z}{R} \in [0.5, 0.75]$) is therefore dependent on complex phase interactions between at least three significant mechanisms. For intermediate positions (roughly $\frac{\Delta X}{R} = 1$, $\frac{\Delta Z}{R} = 1$), the scattering mechanism seems to dominate, with the wing leading edge located in the propeller near field. Finally, the largest separations ($\frac{\Delta X}{R} = 1.5$, $\frac{\Delta Z}{R} = 1.5$) result in lower total installation effects, as all three mechanisms are reduced to within 5 dB. While not exhaustive, the combination of these three interaction mechanisms explains a significant portion of the observed installation effect.

VI. Conclusions

In this work, we present a method for efficient prediction of tonal noise from installed propeller configurations. The method simulates the 3D unsteady flow field with a panel method coupled with a viscous VPM wake model. The acoustic pressure is calculated by computing an incident field with the FWH aeroacoustic analogy and then accounting for the presence of scattering surfaces in the propagation region with a space-time Galerkin TDBEM. The approach therefore models installation effects due to both aerodynamic interactions and scattering without requiring a volume mesh.

The approach is applied to study a propeller-wing configuration originally tested by Zawodny et al. (2021)[1]. Aerodynamic and acoustic predictions are compared with experimental measurements to assess the ability of the present approach to capture the installation effects. Multiple spatial and temporal discretizations are considered to assess sensitivities to resolution. While good agreement is found for mean aerodynamic quantities, a comparison of wing surface pressure fluctuations near the tip vortex path shows significant deviations from experiment that may be related to the inviscid boundary condition in the panel-VPM methodology. Future comparison with a boundary layer-resolving aerodynamic solver is necessary to determine the cause of this discrepancy and its effect on the far-field acoustics.

The predicted and measured SPL directivities are compared at the BPF for several wing positions. These comparisons show important areas of agreement that capture key installation effects, although some discrepancies remain. The components of the predicted solution are decomposed to highlight three physical mechanisms hypothesized to be important in the propeller-wing interaction. Propeller potential flow interaction, wake impingement, and acoustic scattering are all shown to be significant, with similar contribution magnitudes of around 15 dB at the nearest wing position. Both the potential interaction and the wake impingement appear to decrease quickly with increasing separation, although the wake impingement mechanism decreases more slowly for axial separation than for vertical separation. The scattering contribution is found to decrease the slowest, remaining above 15 dB out to vertical and axial separations of one radius. A key finding is the significance of both aerodynamic and acoustic installation effects that must all be included to accurately capture installed propeller noise.

The length scale of the propeller near field is found to have an important effect on the acoustic scattering contribution. Slices of the phase of the propeller pressure field at the BPF show a near-field region with length scales determined by the propeller diameter, extending to about one radius. There is a transition region with intermediate spatial scales between one and four radii, while the spatial scales approach the far-field wavelength beyond four radii. The strong scattering contributions observed for up to one radius of vertical or axial separation are attributed to the short near-field spatial scale, which is over an order of magnitude smaller than the acoustic wavelength. Beyond the propeller near field, the scattering effect decreases substantially as the acoustic spatial scale approaches the wavelength. These observations imply that significant propeller noise scattering may occur from bodies much smaller than the acoustic wavelength if placed in the appropriate part of the incident field. In particular, a scattering body cannot be determined to be acoustically compact on the basis of frequency alone without considering the spatial structure of the propeller acoustic field.

Overall, the present approach appears to have strong potential for computationally efficient prediction of tonal installed propeller noise. Further work will investigate remaining discrepancies between predictions and experimental measurements for both aerodynamic and acoustic quantities and add missing interactional mechanisms such as the self-scattering contribution by the wing. Finally, future work will include additional numerical and geometric parameter studies of propeller-wing configurations, considering variables such as the propeller rotation rate and advance ratio that are not examined in this work.

Acknowledgments

The authors gratefully acknowledge Nikolas Zawodny at the NASA Langley Research Center for providing data and assistance to set up and benchmark the propeller-wing configuration.

References

[1] Zawodny, N. S., Boyd, D. D., and Nark, D. M., "Aerodynamic and acoustic interactions associated with inboard propeller-wing configurations," *AIAA Scitech 2021 Forum*, 2021. https://doi.org/10.2514/6.2021-0714.

[2] Rizzi, S. A., Huff, D. L., Boyd, D. D., Bent, P., Henderson, B. S., Pascioni, K. A., Sargent, D. C., Josephson, D. L., Marsan, M., He, H. B., and Snider, R., "Urban air mobility noise: Current practice, gaps, and recommendations," Technical Publication NASA/TP–2020-5007433, 2020.

[3] Yang, Z., Meinke, M., and Schroeder, W., "Numerical analysis of propeller-airfoil interaction in a distributed propulsion system using a hybrid LES and FW-H approach," *30th AIAA/CEAS Aeroacoustics Conference (2024)*, 2024. https://doi.org/10.2514/6.2024-3211.

[4] Zhou, B. Y., Morelli, M., Gauger, N. R., and Guardone, A., "Simulation and sensitivity analysis of a wing-tip mounted propeller configuration from the workshop for integrated propeller prediction (WIPP)," *AIAA Aviation 2020 Forum*, 2020. https://doi.org/10.2514/6.2020-2683.

[5] Zhou, B. Y., Morelli, M., Dehpanah, P., Gauger, N. R., and Guardone, A., "Aeroacoustic analysis of a wing-tip mounted propeller configuration," *AIAA AVIATION 2021 FORUM*, 2021. https://doi.org/10.2514/6.2021-2224.

[6] Groom, M. J., Wang, Q., and Zhou, B. Y., "A mid-fidelity numerical framework for efficient prediction of propeller-wing interaction noise," *AIAA SCITECH 2022 Forum*, 2022. https://doi.org/10.2514/6.2022-2165.

[7] Ahuja, V., Little, D. S., Majdalani, J., and Hartfield, R. J., "On the prediction of noise generated by urban air mobility (UAM) vehicles. Part II. Implementation of the Farassat F1A formulation into a modern surface-vorticity panel solver," *Physics of Fluids*, Vol. 34, No. 11, 2022, p. 116118. https://doi.org/10.1063/5.0105002.

[8] Barry, K., Pullin, S., Zhou, B. Y., and Lopes de Moraes Filho, L. F., "Mid-Fidelity simulation of a tandem propeller and wing configuration for EVTOL vehicles," *30th AIAA/CEAS Aeroacoustics Conference (2024)*, 2024. https://doi.org/10.2514/6.2024-3041.

[9] Pullin, S. F., Groom, M. J., Zhou, B. Y., and Azarpeyvand, M., "A GPU-accelerated mid-fidelity aerodynamic and aeroacoustic simulation framework," *30th AIAA/CEAS Aeroacoustics Conference (2024)*, 2024. https://doi.org/10.2514/6.2024-3151.

[10] Ffowcs Williams, J. E., and Hawkings, D. L., "Sound generation by turbulence and surfaces in arbitrary motion," *Philosophical Transactions of the Royal Society of London. Series A, Mathematical and Physical Sciences*, Vol. 264, No. 1151, 1969, pp. 321–342. https://doi.org/10.1098/rsta.1969.0031.

[11] Dunn, M. H., "The acoustic analogy in four dimensions," *International Journal of Aeroacoustics*, Vol. 18, No. 8, 2019, pp. 711–751. https://doi.org/10.1177/1475472X19890259.

[12] Romani, G., and Casalino, D., "Application of Lattice-Boltzmann method to rotorcraft aerodynamics and aeroacoustics," *43rd European Rotorcraft Forum*, 2017.

[13] Goldstein, M. E., "A generalized acoustic analogy," *Journal of Fluid Mechanics*, Vol. 488, 2003, pp. 315–333. https://doi.org/10.1017/S0022112003004890.

[14] Yangzhou, J., Wu, J., Ma, Z., and Huang, X., "Aeroacoustic sources analysis of wake-ingesting propeller noise," *Journal of Fluid Mechanics*, Vol. 962, 2023, p. A29. https://doi.org/10.1017/jfm.2023.295.

[15] Proskurov, S., Moessner, M., Ewert, R., Lummer, M., and Delfs, J. W., "Fan noise shielding predictions with a coupled DG/FM-BEM method for installed aircraft engines," *AIAA AVIATION 2021 FORUM*, 2021. https://doi.org/10.2514/6.2021-2167.

[16] Thomas, R. H., and Guo, Y., "Systematic validation of the PAAShA shielding prediction method," *International Journal of Aeroacoustics*, Vol. 21, No. 5-7, 2022, pp. 558–584. https://doi.org/10.1177/1475472X221107369.

[17] Reiche, N., Ewert, R., Lummer, M., and Delfs, J., "Fast multipole boundary element method with stochastic sources for broadband noise simulation," *23rd AIAA/CEAS Aeroacoustics Conference*, 2017. https://doi.org/10.2514/6.2017-3515.

[18] Hu, F. Q., Pizzo, M. E., and Nark, D. M., "On a time domain boundary integral equation formulation for acoustic scattering by rigid bodies in uniform mean flow," *The Journal of the Acoustical Society of America*, Vol. 142, No. 6, 2017, pp. 3624–3636. https://doi.org/10.1121/1.5017734.

[19] Groom, M. J., Pullin, S. F., Zhou, B., and Wang, Q., "A Galerkin time domain boundary element method for scattering and shielding of installed propeller noise," *AIAA SCITECH 2024 Forum*, 2024. https://doi.org/10.2514/6.2024-2810.

[20] Tinetti, A. F., and Dunn, M. H., "The fast scattering code (FSC): Validation studies and program guidelines," Contractor Report NASA/CR-2011-217158, 2011.

[21] Lee, S., Brentner, K. S., and Morris, P. J., "Acoustic scattering in the time domain using an equivalent source method," *AIAA Journal*, Vol. 48, No. 12, 2010, pp. 2772–2780. https://doi.org/10.2514/1.45132.

[22] Lee, S., "The use of equivalent source method in computational acoustics," *Journal of Computational Acoustics*, Vol. 25, No. 01, 2017, p. 1630001. https://doi.org/10.1142/S0218396X16300012.

[23] Tugnoli, M., Montagnani, D., Syal, M., Droandi, G., and Zanotti, A., "Mid-Fidelity approach to aerodynamic simulations of unconventional VTOL aircraft configurations," *Aerospace Science and Technology*, Vol. 115, 2021, p. 106804. https://doi.org/10.1016/j.ast.2021.106804.

[24] Winckelmans, G. S., "Topics in vortex methods for the computation of three- and two-dimensional incompressible unsteady flows," 1989. https://doi.org/10.7907/19HD-DF80.

[25] Pedrizzetti, G., "Insight into singular vortex flows," *Fluid Dynamics Research*, Vol. 10, No. 2, 1992, pp. 101–115. https://doi.org/10.1016/0169-5983(92)90011-k.

[26] Montagnani, D., Tugnoli, M., Fonte, F., Zanotti, A., Syal, M., and Droandi, G., "Mid-fidelity analysis of unsteady interactional aerodynamics of complex VTOL configurations," *45th European Rotorcraft Forum (ERF 2019)*, 2019, pp. 1–11.

[27] Niro, C., Savino, A., Cocco, A., and Zanotti, A., "Mid-fidelity numerical approach for the investigation of wing-propeller aerodynamic interaction," *Aerospace Science and Technology*, Vol. 146, 2024, p. 108950. https://doi.org/10.1016/j.ast.2024.108950.

[28] Savino, A., Cocco, A., Zanotti, A., and Muscarello, V., "Numerical investigation of wing-propeller aerodynamic interaction through a vortex particle-based aerodynamic solver," *48th European Rotorcraft Forum (ERF 2022)*, 2022, pp. 1–9.

[29] Farassat, F., "Derivation of formulations 1 and 1A of Farassat," Technical Memorandum NASA/TM-2007214853, 2007.

[30] Ghorbaniasl, G., Carley, M., and Lacor, C., "Acoustic velocity formulation for sources in arbitrary motion," *AIAA Journal*, Vol. 51, No. 3, 2013, pp. 632–642. https://doi.org/10.2514/1.J051958.

[31] Lockard, D., "A comparison of Ffowcs Williams-Hawkings solvers for airframe noise applications," *8th AIAA/CEAS Aeroacoustics Conference & Exhibit*, 2002. https://doi.org/10.2514/6.2002-2580.

[32] Casalino, D., "An advanced time approach for acoustic analogy predictions," *Journal of Sound and Vibration*, Vol. 261, No. 4, 2003, pp. 583–612. https://doi.org/10.1016/S0022-460X(02)00986-0.

[33] Hu, F. Q., Pizzo, M. E., and Nark, D. M., "On the use of a Prandtl-Glauert-Lorentz transformation for acoustic scattering by rigid bodies with a uniform flow," *Journal of Sound and Vibration*, Vol. 443, 2019, pp. 198–211. https://doi.org/10.1016/j.jsv.2018.11.043.

[34] Taylor, K., "A transformation of the acoustic equation with implications for wind-tunnel and low-speed flight tests," *Proceedings of the Royal Society of London. A. Mathematical and Physical Sciences*, Vol. 363, No. 1713, 1978, pp. 271–281. https://doi.org/10.1098/rspa.1978.0168.

[35] Mancini, S., Astley, R. J., Sinayoko, S., Gabard, G., and Tournour, M., "An integral formulation for wave propagation on weakly non-uniform potential flows," *Journal of Sound and Vibration*, Vol. 385, 2016, pp. 184–201. https://doi.org/10.1016/j.jsv.2016.08.025.

[36] Ha-Duong, T., "On retarded potential boundary integral equations and their discretisation," *Topics in Computational Wave Propagation: Direct and Inverse Problems*, 2003, pp. 301–336. https://doi.org/10.1007/978-3-642-55483-4_8.

[37] Alain, B., and Ha-Duong, T., "Formulation variationnelle pour le calcul de la diffraction d'une onde acoustique par une surface rigide," *Mathematical Methods in the Applied Sciences*, Vol. 8, No. 1, 1986, pp. 598–608. https://doi.org/10.1002/mma.1670080139.

[38] Burton, A., and Miller, G., "The application of integral equation methods to the numerical solution of some exterior boundary-value problems," *Proceedings of the Royal Society of London. A. Mathematical and Physical Sciences*, Vol. 323, No. 1553, 1971, pp. 201–210. https://doi.org/10.1098/rspa.1971.0097.

[39] Chappell, D., and Harris, P., "On the choice of coupling parameter in the time domain Burton–Miller formulation," *The Quarterly Journal of Mechanics & Applied Mathematics*, Vol. 62, No. 4, 2009, pp. 431–450. https://doi.org/10.1093/qjmam/hbp018.

[40] Yu, K. H., Kadarman, A. H., and Djojodihardjo, H., "Development and implementation of some BEM variants—A critical review," *Engineering Analysis with Boundary Elements*, Vol. 34, No. 10, 2010, pp. 884–899. https://doi.org/10.1016/j.enganabound.2010.05.001.